Stabilizing Edge-Fluorination in Graphene Nanoribbons

Mirco Panighel,[*,†,⊥] Sabela Quiroga,[‡] Pedro Brandimarte,[¶] Cesar Moreno,[†] Aran Garcia-Lekue,[¶,§] Manuel Vilas-Varela,[‡] Dulce Rey,[‡] Guillaume Sauthier,[†] Gustavo Ceballos,[†] Diego Peña,[*,‡] and Aitor Mugarza[*,†,‖]

†*Catalan Institute of Nanoscience and Nanotechnology (ICN2), CSIC and The Barcelona Institute of Science and Technology, Campus UAB, Bellaterra, 08193 Barcelona, Spain.*

‡*Centro de Investigación en Química Biolóxica e Materiais Moleculares (CiQUS) and Departamento de Química Orgánica, Universidade de Santiago de Compostela. Santiago de Compostela 15782, Spain.*

¶*Donostia International Physics Center, Paseo M. de Lardizabal 4, 20018 San Sebastian, Spain.*

§*Ikerbasque, Basque Foundation for Science, 48013 Bilbao, Spain.*

‖*ICREA Institució Catalana de Recerca i Estudis Avançats, Lluis Companys 23, 08010 Barcelona, Spain.*

⊥*Current address: CNR-IOM Laboratorio TASC, SS 14 km 163.5 - Basovizza, I-34149 Trieste, Italy.*

E-mail: panighel@iom.cnr.it; diego.pena@usc.es; aitor.mugarza@icn2.cat

Abstract

The on-surface synthesis of edge-functionalized graphene nanoribbons (GNRs) is challenged by the stability of the functional groups throughout the thermal reaction

steps of the synthetic pathway. Edge-fluorination is a particularly critical case, where the interaction with the catalytic substrate and intermediate products can induce the complete cleavage of the otherwise strong C-F bonds before the formation of the GNR. Here, we demonstrate how a rational design of the precursor can stabilize the functional group, enabling the synthesis of edge-fluorinated GNRs. The survival of the functionalization is demonstrated by tracking the structural and chemical transformations occurring at each reaction step with complementary X-ray photoelectron spectroscopy and scanning tunneling microscopy measurements. In contrast to previous attempts, we find that the C-F bond survives the cyclodehydrogenation of the intermediate polymers, leaving a thermal window where GNRs withhold more than 80% of the fluorine atoms. We attribute this enhanced stability of the C-F bond to the particular structure of our precursor, which prevents the cleavage of the C-F bond by avoiding interaction with the residual hydrogen originated in the cyclodehydrogenation. This structural protection of the linking bond could be implemented in the synthesis of other sp^2-functionalized GNRs.

Keywords

graphene nanoribbons, on-surface synthesis, edge-functionalization, fluorination, scanning tunneling microscopy, density functional theory, self-assembly

The functionalization of graphene nanoribbons (GNRs) is an effective method for tailoring their structural, chemical and electronic properties[1–10]. Edge functionalization by replacing hydrogen with different substituents is particularly interesting since it offers a wide flexibility in the choice of functional groups that can, in addition to band tuning,[1] bring chemical selectivity for sensing.[8] Their peripheral position can also be employed to tune inter-ribbon and substrate interactions and drive their organization, one of the most important challenges in bottom-up synthetic methods.[7,11,12] The atomic precision offered by bottom-up synthetic methods in the positioning of each component makes this approach the

natural candidate for a controlled functionalization of the ribbons. The thermally activated sequential on-surface synthesis has shown to be particularly effective for the realization of atomically precise GNRs[13–15]. However, such multi-step methods also face a major challenge, namely the stability of the functional groups that have to overcome the whole reaction pathway that leads to the GNR synthesis. This is critical in the functionalization of edges, where the linking groups are not as strongly bound to the aromatic backbone as hetero-atoms in substitutional doping. In the absence of stabilizing intra- or inter-ribbon reactions,[3,6,7] the thermal energy supplied during the synthesis can surpass the linking bond energy, leading to a partial[4] or a total[16] dissociation of the functional groups. Dissociation can occur even in carefully chosen, strongly bonded groups, since the intermediate products formed during the reaction pathway can destabilize the bond between the carbon backbone and the functional group, and induce a premature cleavage. This was recently shown in an attempt to synthesize edge-fluorinated GNRs, where it was found that the activation barrier of the otherwise strong C-F bond was reduced by one order of magnitude, mainly by the formation of an additional C(sp^3)-H bond with residual H migrating from nearest neighbor C atoms during the cyclodehydrogenation (CDH) step.[16] The understanding of this C-F cleaving mechanism can be used for the rational design of fluorinated precursors that avoid the formation of undesired, destabilizing transient structures, as explicitly stated by the authors. Here, we demonstrate how a suitable design of the molecular precursor can lead to the successful synthesis of edge-fluorinated GNRs. These are synthesized on a Au(111) single crystal in a step-wise thermal process, initially *via* the surface-assisted Ullmann coupling of the fluorinated monomers into polymeric chains and then through the subsequent CDH leading to the formation of the graphene nanoribbons.[17] The functionalized precursors have been specifically synthesized to overcome these thermally activated reaction steps. The key element in the design is the separation between the fluorinated carbon and those involved in the CDH reaction, which minimizes the defluorination rate by introducing new paths for residual H release onto the surface. Regarding the electronic properties of the functionalized GNRs,

our *Ab Initio* calculations reveal a significant *n*-type doping effect of fluorination, shifting frontier bands downwards by about 200 meV and leaving the size of the gap unchanged. The doping effect, however, can be fully screened out by the interaction with the metallic substrate, as demonstrated by both *Ab Initio* and scanning tunneling spectroscopy results.

Results and discussion

First, we designed a GNR precursor core which could allow us the easy introduction of different functional groups in peripheral positions, with the goal to minimizing the possible group cleavage during the CDH step. With this idea in mind, we selected the benzo[*b*]triphenylene core which is presented in compounds **1a,b** (Figure 1a), including two Br atoms to induce the on-surface Ullmann coupling to form polymers **2a,b** and two phenyl groups to facilitate the CDH step to obtain GNRs **3a,b**. These GNRs resemble the previously reported chevron GNR,[17] although **3a,b** are narrower and characterized by the combination of cove and triple-bay regions along the edges. Besides the unsubstituted GNR **3a** (R = H) we planned to obtain the fluorinated GNR **3b** (R = F). Remarkably, these GNRs were designed with the functional groups attached to remote positions with respect to the carbon atoms involved in the CDH step, in order to minimize the potential weakening and subsequent cleavage of these groups. Precursors **1a,b** were easily obtained by solution chemistry, in three steps from commercially available reagents (Figure 1b). First, bromination of 9,10-phenanthroquinone (**4**) followed by double Knoevenagel condensation with 1,3-diphenylacetone afforded dienone **5** in good yield. Then, Diels-Alder reaction of **5** with arynes **6a,b** which were *in-situ* generated by fluoride-induced decomposition of triflates **7a,b** led to the formation of benzo[*b*]triphenylenes **1a,b** after CO extrusion of the corresponding adducts.

With compounds **1a,b** in hands, we launched the on-surface studies to attempt the preparation of GNRs **3a,b** on Au(111). The formation of the expected GNRs and the stability of the functional groups throughout the on-surface synthetic protocol have been investigated by

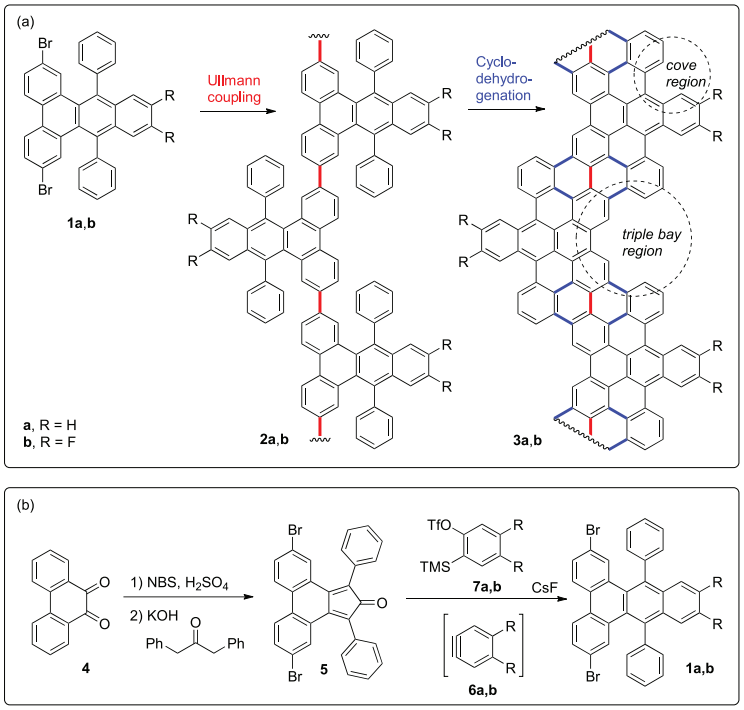

Figure 1: (a) On-surface synthesis of GNRs **3a,b** (b) In-solution synthesis of benzo[*b*]triphenylene derivatives **1a,b** used as GNR precursors.

complementary scanning tunneling microscopy (STM) and X-ray photoelectron spectroscopy (XPS) measurements. Exploiting the chemical sensitivity of XPS, the reactions resulting in the synthesis of the GNRs have been systematically characterized, as summarized in Figure 2. After depositing compounds **1a,b** at room temperature (RT) and annealing at 200 °C, these GNR precursors undergo a C-Br homolytic bond cleavage, leading to the formation of aryl radicals and the subsequent coupling into polymeric chains **2a,b** *via* the Ullmann coupling. Figure 2a shows the XPS spectra of the Br 3d core levels for precursor **1b** (R = F). The binding energy of the spin-orbit split doublet measured for precursors deposited at RT, 69.9/70.9 eV, corresponds to the C-bonded Br. The doublet downshift by 2.1 eV upon annealing at 200 °C can be assigned to C-Br cleavage and consequent formation of Au-bonded Br adsorbates.[18–20] The completion of the C-Br cleavage is in agreement with the Ullmann polymerization observed by STM at the same temperature (Figure 3). At higher temperature, Br adatoms desorb from the surface, as indicated by the absence of any Br 3d peak

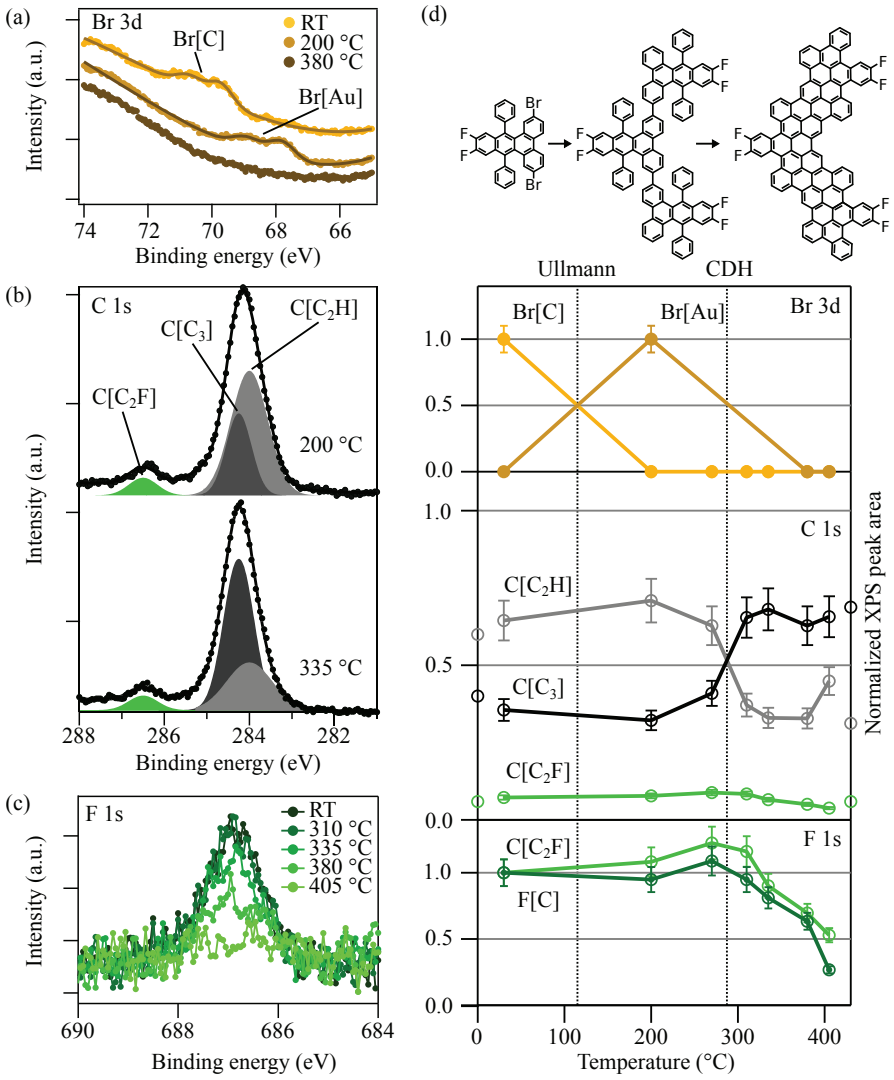

Figure 2: (a)-(c) XPS core level spectra of Br 3d (a), C 1s (b), and F 1s (c) after annealing precursor **1b** at different temperatures. The C 1s spectra fit (continuous lines) is done with multiple peaks to account C[C_3], C[C_2H] and C[C_2F] contributions. (d) Thermal evolution of the XPS atomic ratios, normalized against gold, of the different peaks in (a)-(c). The vertical lines indicate the Ullmann and CDH reaction steps of the GNR synthesis, as indicated by the respective changes in Br[C]/Br[Au] and C[C_3]/C[C_2H] ratios. In the C 1s series, the open circles at the left and right limits represent the stoichiometric relation of the different components for the precursors and the nanoribbons respectively. A normalized C[C_2F] curve has been added to the F[C] data of F 1s.

in the spectrum obtained after annealing at 380 °C. This is clearly visible also in Figure 2d which reports the thermal evolution of the XPS atomic ratios of the different peaks normalized against gold. The CDH reaction that convert polymers **2** into GNRs **3** can be tracked by following the temperature evolution of the C 1s core level components. As representative examples, Figure 2b shows the C 1s core level XPS spectra after annealing **1b** at 200 °C and 335 °C, illustrating the evolution of C bond ratios that correspond to the CDH step. The main C peak is best fitted with two components that can be assigned to C[C_3] (284.3 eV) and C[C_2H] (284.0 eV) bonds respectively. The minor C-Br component is only present at RT according to the Br 3d peak evolution, and therefore is not considered in this analysis. The additional peak present at higher binding energies accounts for the C[C_2F] (286.5 eV) bond component. As we increase the annealing temperature, a clear inversion of the C[C_3] and C[C_2H] components is visible around 300 °C. This is evident in Figure 2d which reports the thermal evolution of the XPS peak area related to the different components. By comparing to the stoichiometric references of the polymeric and GNR phases indicated at the two sides of the graph by open circles, this transition of the C[C_3]/C[C_2H] ratio corresponds to the cyclodehydrogenation that leads to the formation of GNRs at this temperature, as also confirmed by the STM measurements (Figure 3). The relevant features regarding the stability of the functional group are the C[C_2F] component of C 1s and the correlated F 1s peaks. The evolution of the latter is reported in Figure 2c for the whole set of temperatures investigated. Interestingly, the C[C_2F] bond survives well above the CDH threshold. As can be seen in detail in Figure 2d, the intensity of the C[C_2F] components of C 1s and the F[C] of F 1s remains unaltered during the formation of GNRs at 310 °C, and still withhold 80% of the intensity at 335 °C when the CDH is complete. Their gradual decrease down to about ~25% at the maximum studied temperature of 405 °C is accompanied by an increase of the C[C_2H] component above the stoichiometric ratio of **3b**, suggesting that cleaved C radicals are passivated by residual H.

We next compare the XPS spectroscopic analysis with the structural information provided

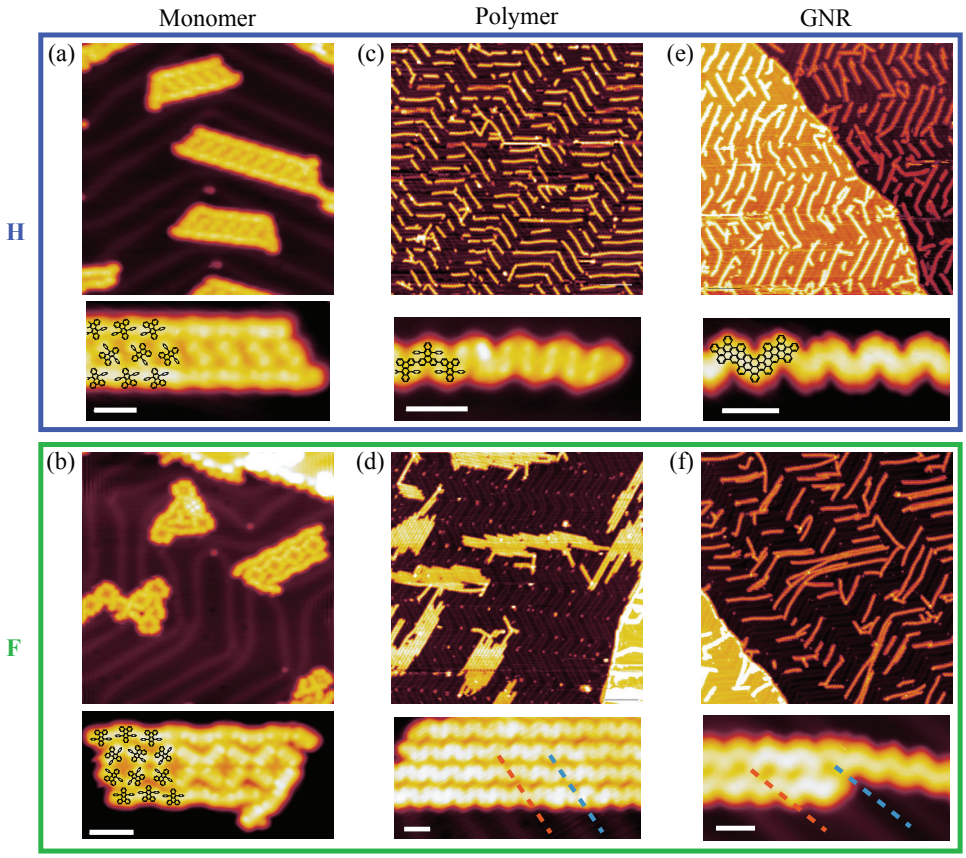

Figure 3: STM images of the hydrogenated (**1a**) and fluorinated (**1b**) precursors and corresponding polymeric chains and GNRs. (a) Precursor **1a** deposited at room temperature. (I_t = 160 pA, V_s = 1.39 V. Inset: I_t = 160 pA, V_S = 1.39 V). (b) Precursor **1b** deposited at room temperature. (I_t = 96 pA, V_s = 1.09 V. Inset: I_t = 290 pA, V_S = 1.28 V). (c) Polymer **2a** after annealing at 225 °C (I_t = 85 pA, V_s = 1.36 V. Inset: I_t = 130 pA, V_s = 1.75 V). (d) Polymer **2b** after annealing at 225 °C (I_t = 46 pA, V_s = 2.52 V. Inset: I_t = 60 pA, V_s = 1.28 V). (e) GNR **3a** after annealing at 400 °C (I_t = 75 pA, V_s = 1.36 V. Inset: I_t = 250 pA, V_s = -0.1 V). (f) GNR **3b** after annealing at 335 °C (I_t = 80 pA, V_s = 1.30 V. Inset: I_t = 210 pA, V_s = 1.23 V). The surface stacking domains of the Au(111) herringbone reconstruction are marked with red (face-centered cubic, fcc) and cyan (hexagonal closed packed, hcp) dashed lines. Images size is 25.6x25.6 nm^2 for (a,b) and 150x150 nm^2 for (c-f). All inset scale bars correspond to 2 nm.

by STM at each reaction step. Figure 3 shows representative STM topographic images for **1a** (R = H) and **1b** (R = F) deposited at room temperature, and the corresponding polymeric chains and GNRs synthesized in each reaction step. In both cases, annealing at 200 °C leads to the Ullmann polymerization of precursors into chains with a zig-zag backbone of an apparent height of 0.2 nm, and protrusion pairs with a center-to-center distance of 0.8 nm. The comparison of the polymeric unit structure with the precursor monomer confirms that the double protrusions correspond to the out-of-plane phenyl rings and that functional groups stay on the protruding edge of the zig-zag backbone (see insets in Figure 3c,d). Further annealing (at 335 °C for F-GNR and 400 °C for H-GNR) leads to the formation of planar chevron-type structures (insets in Figure 3e,f), as expected from the incorporation of the side phenyl rings into the backbone after the CDH reaction. The overall apparent height of 0.15 nm of this structure is in good agreement with previously reported GNRs[17,20] (cross-sectional line profiles of the apparent height of polymers and GNRs are provided in Fig. S7).

Despite their similar intra-molecular structural evolution, the substituents of each precursor leads to inter-molecular interactions that dictate distinct assembly patterns. This is evident from the initial monomeric phase at room temperature (Figures 3a and b). For **1a** the interaction with the substrate is strong enough to constrain the self-assembly within the more favourable fcc tracks of the herringbone reconstruction of the Au(111) surface. In contrast, the stronger interactions between the fluorinated **1b** monomers lead to self-assembled structures that, although still guided by the underlying surface reconstruction, surpass the fcc/hcp domain boundaries. In the intermediate polymeric phase, the morphological differences are even more dramatic (Figures 3c and d). In the case of **2a** the herringbone reconstruction guides the polymer assembly. The single chains fill the fcc tracks, terminating at the kinks of the herringbone zigzag, and hence giving rise to a superlattice of chains with a narrow length distribution that is determined by the zigzag period. Instead, F-mediated inter-chain interactions for **2b** are strong enough to bunch them in parallel arrays that ap-

pear off-registry with the herringbone template, avoiding any size restriction imposed by it. The differences are minimized after the aromatization of the polymers into GNRs (Figures 3e and f). In this step, **3a** GNRs simply replicate the polymer superlattice, whereas the stronger interaction of the planar structures with the substrate causes a debunching of **2b** polymeric arrays into single **3b** GNRs that now try to follow the herringbone reconstruction. The overgrown GNRs, however, do not fit in the zigzag units of the reconstruction and consequently the quality of the superlattice is significantly reduced.

A deeper insight into the conformation of the cove regions that surround the functionalized benzene indicates that they cannot withhold a coplanar structure due to the steric repulsion between the hydrogens of adjacent rings. One way to overcome this steric repulsion is by a dehydrogenative closure of the cove into a pentagonal ring (Figure S8c). This configuration is, however, 7.10 eV less stable than the structures that only involved conformational changes, and is therefore not likely to form. For free standing ribbons at T=0, we find two configurations where steric hindrance is avoided by tilting the functionalized ring along the pitch axis (upwards/downwards, see Figure S8a) or the roll axis (sideways, see Figure S8b). The former is slightly more stable, with an energy difference of 0.56 eV. On the Au(111) surface, the symmetry reduction splits the first configuration into two, leading to a total of three configurations (Figure 4b): one with the fluorinated ring up (F_{up}), another down (F_{down}), and a third one sideways (F_{side}). The three still remain quasidegenerate, with an energy difference between F_{up} and F_{down} as low as 0.25 eV. High resolution STM images provide evidences of the presence of the three conformations, as shown in Figure 4. In images acquired at bias voltages in the valence band (VB) region we find that most fluorinated rings have low contrast, but some exhibit one or two side protrusions. The same protrusions are found for **3a**, excluding any specific relation to the fluorine atoms (Figure S6). We attribute these protrusions to the tilt of the fluorinated ring, and accordingly assign the dominant low contrast units to the F_{down} configuration, and the single and double side protrusions to the F_{side} and F_{up} configurations respectively. Such assignment is supported by comparing STS

maps obtained at the VB and conduction band (CB) regions with wave functions obtained by density functional theory (DFT) at these energies (Figure 4e-d). In the STS maps, side protrusions found at the VB energy convert into a single centered bright protrusion at the CB energy (Figures 4c-e). This corresponds nicely with the symmetry of the corresponding wavefunctions at the VB maximum and CB minimum located at the Γ point, where STM is most sensitive. At the functionalized ring, the wavefunction of the VB exhibits a nodal plane transversal to the ribbon, whereas that of the CB has a single maxima centered at the ring.

From the STM images, as the one shown in Figure 4a, we estimate that around 90% of the fluorinated rings remain in the F_{down} configuration. The prevalence of this configuration can be explained by considering the initial configuration before the CDH of the polymer. Here, the fluorinated ring is already in direct interaction with the surface. The tilted side phenyls can in principle rotate in either direction in order to fuse to the backbone by CDH (blue lines in Figure 1a), each leading to one of the two (F_{up}/F_{down}) configurations. For the rotation direction that leads to a final F_{up} configuration, the steric repulsion between the side rings have to counteract the interaction of the fluorinated ring with the substrate in order to lift the latter. This additional barrier is expected to break the degeneracy and favour the F_{down} configuration.

The stability of **3b**, the chevron-type fluorinated GNR synthesized in this work, is in contrast to previous attempts of synthesizing edge-fluorinated armchair GNRs using different anthracene derivatives as precursors.[16,21] In these cases polymers were fully defluorinated before turning into GNRs. With the C-F bond being one of the strongest C-heteroatom single bond, the premature cleavage was unexpected and attributed to a combination of surface and byproduct assisted bond weakening. According to the DFT calculations,[16] the interaction with the underlying Au atoms already reduces the activation energy of the C(sp^2)-F bond cleavage by 100 kJ/mol. A more significant weakening is induced by the sp^3 bonding of a residual H generated in the nearest neighbor C atom during the CDH, which brings the

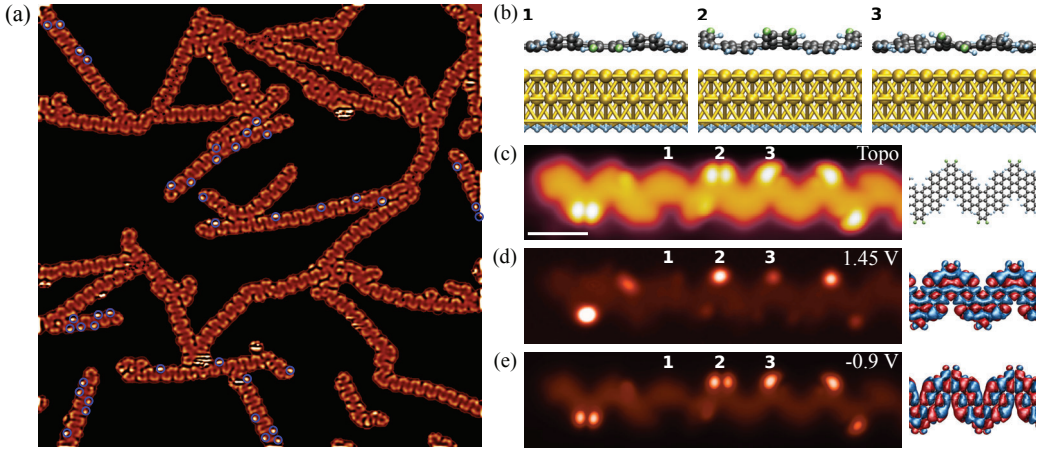

Figure 4: (a) High-pass filtered STM image of F-GNR **3b** after annealing at 335 °C. About 90% of the configuration is F_{down} and about 10% (encirlced in blue) is F_{up}/F_{side} (Image size 60x60 nm^2. I_t = 100 pA, V_s = 1.40 V). (b) Three different configurations obtained after relaxation on Au(111) surface. (c) High resolution STM image of **3b** in which the three configuration can be identified: (1) F_{down}, (2) F_{up}, (3) F_{side} (Scale bar 2 nm. I_t = 100 pA, V_s = -0.9 V). Related dI/dV conductance maps at (d) + 1.45 V and (e) -0.9 V, together with wave functions relative to configuration (2) F_{up} at the CB minimum (d) and VB maximum (e). Wave functions are plotted for a constant amplitude isosurface of 0.005 Bohr$^{-3/2}$, where the colors indicate the phase.

activation energy further down by 400 kJ/mol. Altogether, the two effects reduce the C-F cleavage activation energy close to an order of magnitude, from ~540 kJ/mol to ~40 kJ/mol.

We studied the C-F bond stability of **3b** by performing DFT calculations for the gas-phase and on-surface F_{down} configurations (Figure 5a). In the gas-phase, C(sp^3)-H bond formation leads to a similar reduction of ~400 kJ/mol of the C-F bond cleavage energy, from 554 kJ/mol in C(sp^2)-F to 152 kJ/mol in H-C(sp^3)-F, indicating that the local environment is the most important factor determining the stability of these bonds. We also find that for H-C(sp^3)-F, defluorination is favorable over dehydrogenation by 75 kJ/mol. On the surface, the bond cleavage energies are reduced considerably, as expected from the catalyitic role of Au(111), but the trend is maintained. Defluorination in the absence of residual H is still exothermic with an energy cost of 169 kJ/mol. In contrast, H and F dissociation in the H-C(sp^3)-F transient turn slightly endothermic, defluorination being still favoured by 43 kJ/mol. The main conclusion of this analysis is that the C-F bond in the H-C(sp^3)-F

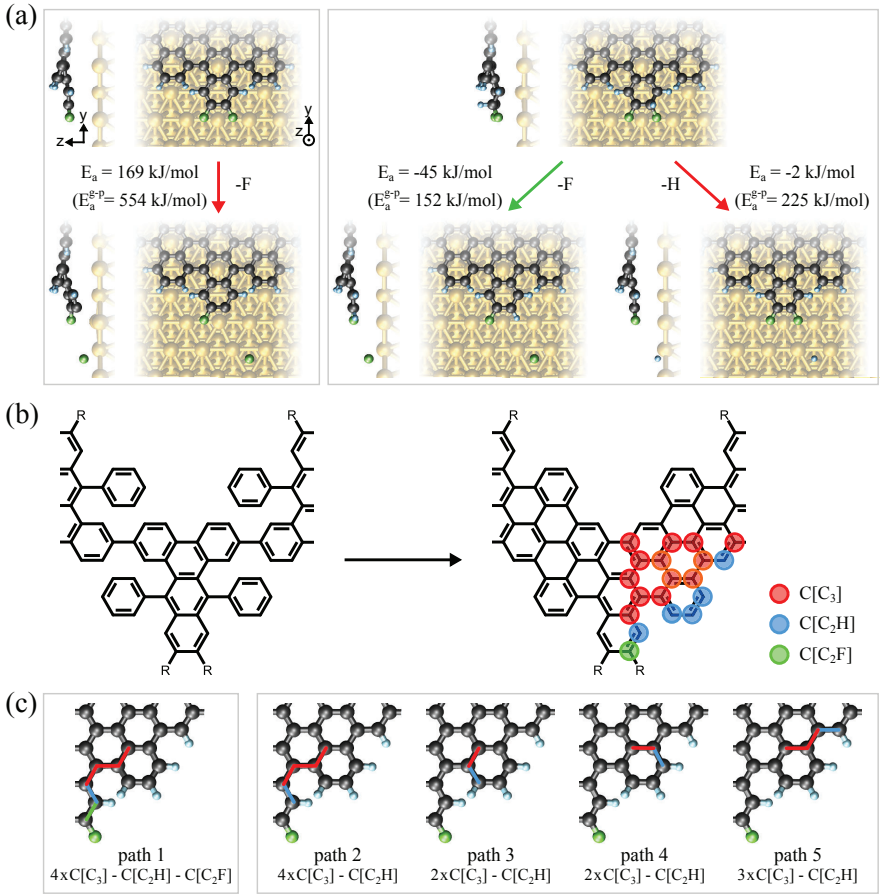

Figure 5: Stability analysis of the C-F bond. (a) Calculated dissociation energies of the C(sp^2)-F bond (left) and of C-H and C-F bonds within the H-C(sp^3)-F group (right). Values in parenthesis refer to the correspondent gas-phase values (see Figure S9). (b) The three different families of C(sp^2) atoms depending on their local environment in the GNR sub-unit. (c) Possible migration paths of the closest H atom towards the edge C, marked with the color code of the families in b.

group is not more stable in the chevron GNRs of the present work than in the armchair GNRs described in Ref. 13. The difference between the two cases lies in the probability of obtaining the transient H-C(sp^3)-F configuration. Since migration barriers are expected to be similar for different ribbon topologies, the formation rate of the H-C(sp^3)-F group will mainly depend on the specific sites where residual H are originated during the CDH reaction with respect to the fluorinated C position. For the armchair GNRs described in Ref. 13, H is released from the vicinal C atom, and a low migration energy barrier of ~80 kJ/mol to the fluorinated C atom results in a high formation rate of the transient H-C(sp^3)-F configuration (k~10^7 s^{-1} at 400 °C). In contrast, the particular design of our precursor relocates the closest formation of residual H significantly further away, at the 5th nearest neighbor (Figure 5b and path 1 in Figure 5c). This introduces new low activation barrier paths for the release of the residual H into the surface *via* the hydrogenated C edge atoms, effectively preventing the formation of the H-C(sp^3)-F groups and therefore the corresponding defluorination. In our analysis of H release paths, we only consider residual H generation closest to the C-F bond, noting that the others only differ by additional migration steps within the GNR backbone. This originates from the cleavage of the C-H pair marked in orange circles in the polymer of Figure 5b. Each pair produces one C(sp^3)-H after the C-C coupling, since the C-H pointing downwards is directly released to the surface.[16,22] In total, we find 5 possible paths from this initial position of the residual H to the nearest C edge atoms, which are sketched in Figure 5c. The color of the segments in each path indicates hopping to three different carbon types, C[C_3], C[C_2H] and C[C_2F], corresponding to fully carbon-bonded, hydrogenated and fluorinated edge atoms respectively (Figure 5b). Path 1 is the one inducing defluorination by the mechanism proposed in Ref. 13, whereas paths 2-5 reach hydrogenated edge C atoms that can release the residual H to the surface by an equivalent dehydrogenation process.[22] A common property shared by both fluorinated and hydrogenated edges is that, in the presence of a C(sp^3)-H bond, they are both characterized by an activation energy for C-F and C-H bond cleavage that is significantly smaller than the migration barrier of the residual H to

the vicinal C.[16,22] The probability ratio between C-F and C-H cleavage will then exclusively depend on the probability of arrival of the residual H to the corresponding edge C atom. This is effectively reduced by the topology of **3b** in two ways: providing multiple additional paths for H release (paths 2-5) and, more importantly, interposing one of these paths (path 2) to the defluorination one (path 1). Altogether, the precursor design effectively prevents defluorination during the synthesis, as demonstrated directly by the temperature dependent XPS measurements.

Some effects of fluorination are imprinted in the electronic properties of the free-standing GNR, despite the apparent low density of edge fluorination exhibited by **3b**. DFT calculations of the gas-phase structure reveal a significant downshift of valence and conduction bands of ~200 meV (Figure 6a), which can be seen as an electrostatic *n*-gating induced by the electron accumulation at the fluorine atoms. As opposed to fully edge-halogenated armchair[1] and cove[2] GNRs, the size of the band gap is barely affected by the fluorination (1.48/1.49 eV in gas-phase for **3a**/**3b** respectively), probably due to the lower nominal density of edge-fluorination and different topology of our chevron GNRs. Indeed, a similar quasi-rigid downshift have been also observed in N-doped chevron GNRs.[23,24] The band shift of **3b** is reduced to negligible values (~10 meV) when GNR interacts with the Au substrate, as can be noted from the projected density of states (PDOS) plotted in Figure 6b. We attribute this band realignment to interfacial charge redistribution, similar to that leading to the Fermi level pinning in armchair GNRs.[25] An additional effect of the surface is the reduction of the band gap from ~1.5 eV to 1.3 eV for free-standing and on-Au GNRs respectively, which is attributed to hybridization with Au states. The absence of any sizeable band gap difference and shift is reproduced in comparative spectroscopic measurements performed in **3a** and **3b** GNRs on the Au substrate (Figure 6c). Here we find the onset of the VB fixed at -0.91 eV for both GNRs, whereas the onset of the CB can be identified at 1.05 eV for **3a** and 0.95 eV for **3b**. The resulting gaps of 1.96 eV and 1.86 eV are slightly larger than the 1.3 eV obtained by DFT, which is accounted by the well-known gap underestimation of this

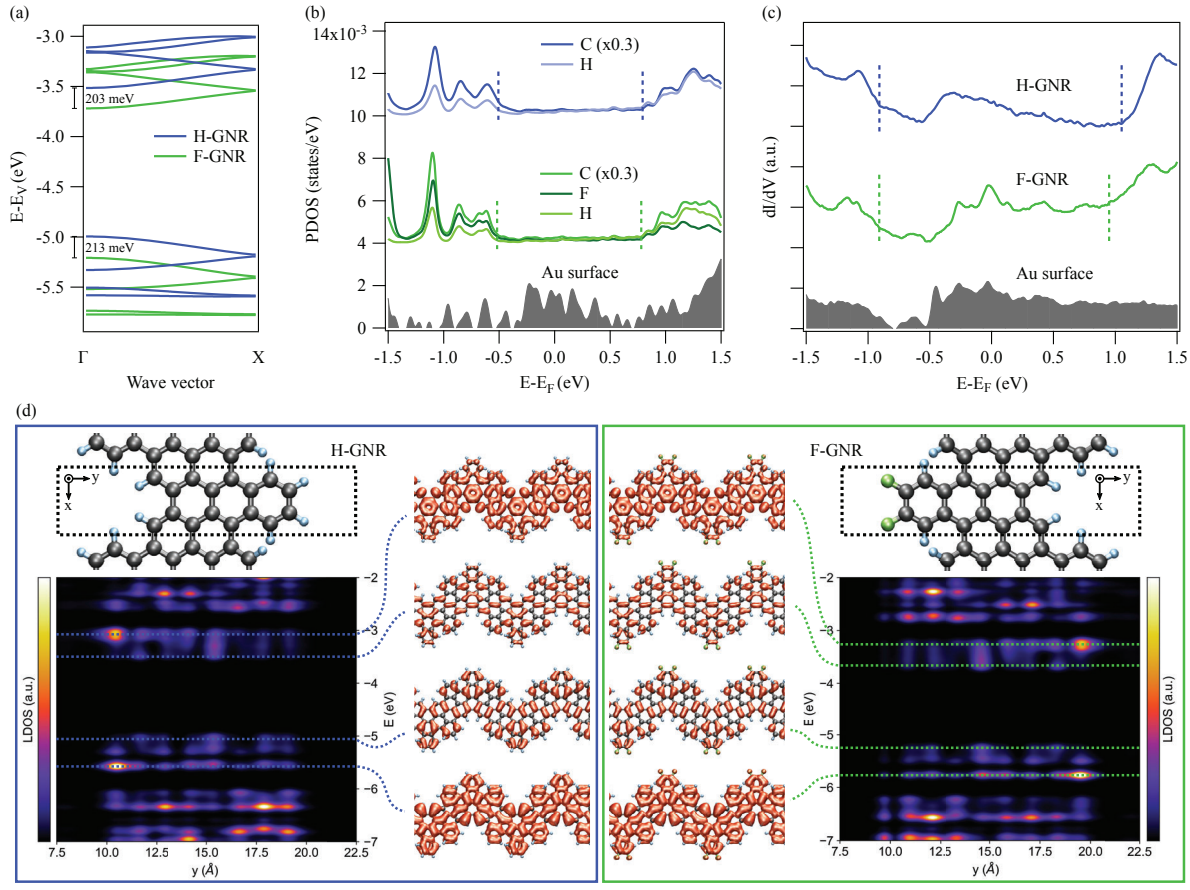

Figure 6: Electronic structure of the GNRs **3a,b**. (a) Band structures of free-standing **3a** (H-GNR, blue) and **3b** (F-GNR, green) for the structures relaxed on Au(111). Energies given with respect to the vacuum energy. (b) PDOS on the different chemical species from **3a** (blue curves, top) and from **3b** (green curves, middle), both calculated on a Au(111) substrate and with a Lorentzian broadening of 35 meV. The PDOS on the surface Au atoms far from the GNR is shown in shaded gray at the bottom (see Methods). (c) Representative constant-height dI/dV spectra taken on **3a** (after CDH at 400 °C) and **3b** (after CDH at 335 °C) in the position of the functional group. Spectrum taken on clean Au is reported in shaded gray as reference. (d) Local density of states of the boxed regions (dashed black) as a function of energy (integrated at energy windows of 20 meV) and integrated along x and z directions, for gas-phase **3a** (left) and **3b** (right). Some representative LDOS isosurfaces ($3.5\text{x}10^{-4}$ e/Bohr^3) obtained by integrating around specific energies ($\pm$ 50 meV) within the region explored experimentally are shown.

method.[26]

In the energy range of ± 1.5 eV that could be explored by scanning tunneling spectroscopy in a stable manner, we find no clear signatures related to edge fluorines. This is confirmed by DFT using spatially resolved local density of states (LDOS), where charge localization can be best visualized. Fig. 6d compares a combination of cross-sectional LDOS and charge density maps of **3a** and **3b**. The cross-sectional LDOS is computed across the ribbon, averaged within the box drawn in the schematic model. Full charge density maps are extracted for some representative states within the energy region explored experimentally. The charge densities of both GNRs in the occupied and unoccupied region are indistinguishable. Only by moving 1 eV below the VB some weak charge density can be inferred at fluorine atoms, as shown by the cross-sectional DOS. For tunneling spectroscopy, that would mean going below $\sim \pm$ 2 eV with bias voltage, which is beyond the stability energy window found in the experiments.

Conclusion

We have demonstrated the on-surface synthesis of edge-fluorinated GNRs. Our combined thermal evolution study of XPS and STM measurements provides chemical and structural evidences of the formation of chevron type GNRs and the survival of fluorine functionalization throughout the whole synthetic path. As opposed to the case of armchair type GNRs based on fluorinated anthracene derivatives (DBTA), where the polymers are fully defluorinated before the formation of GNRs, we achieve 100% of fluorination at the threshold of GNR formation. In a thermal window of 40 °C above that threshold we only observe a slight decrease to 80%. According to first-principle calculations, the electronegative fluorine atoms tend to shift the valence and conduction bands of free-standing GNRs to lower binding energies by about 200 meV without affecting the size of the gap. However, this shift is canceled out in the experimental dI/dV spectra due to the pinning effect of the underlying metallic substrate. The stability of the fluorine substituents is attributed to the particular

design of the precursor, in which the F atoms are introduced in remote positions with respect to the cyclodehydrogenation regions. By providing alternative H release paths, our design effectively hampers the migration of residual H originated during cyclodehydrogenation to the fluorinated C edge atom, and the consequent formation of the H-C(sp^3)-F bond that facilitates the C-F bond cleavage. These alternative H release pathways are independent of the functional group, and hence we expect that our approach should enable the synthesis of other edge-functionalized GNRs. The structural origin of the stabilization highlights the relevance of a rational design of precursors not only for achieving a particular topology of the final product but also for defining reaction pathways that avoid destabilizing transient structures.

The Supporting Information available online contains the details of the molecular synthesis and additional theoretical and experimental details on GNRs structure.

Methods

STM and XPS measurements were performed in two separated ultra-high vacuum (UHV) systems with a base pressure below $5x10^{-10}$ mbar. Clean Au(111) samples were prepared by cycles of Ar ion sputtering at 1 keV and annealing at 470 °C for 20 minutes. Surface cleanliness has been checked by low energy electron diffraction (LEED) and either STM or XPS. Molecular precursors have been deposited from a resistively heated crucible on the Au(111) substrate kept at RT. For the sub-monolayer coverage studied, **1a** and **1b** were sublimated at 280 °C and 300 °C respectively. The sample was annealead at a rate of about 1 °C/s and kept 15 minutes at the indicated temperatures to promote the polymerization and cyclodehydrogenation reactions. Sample temperatures were measured with an infrared pyrometer in the XPS setup and a thermocouple directly spot-welded on the sample holder in the STM setup. The pyrometer was previously calibrated with the sample holder thermocouple of the STM setup in order to have reliable temperature comparison between the two measuring

methods. STM measurements have been carried out with a Createc LT-STM operated at samples temperatures of 5 K, except for the image of the inset of Figure 3c, which was acquired at 77 K . STM topographic images have been acquired in constant-current mode and analyzed and processed with Gwyddion software.[27] STM dI/dV spectra and conductance maps have been measured at 5 K in constant-height mode with the lock-in technique and a bias modulation of 20 mV at 3 kHz. Due to the difficulty of determining the VB/CB maxima/minima in the broad experimental features, both the theoretical and experimental band gaps have been determined by considering the onset of the corresponding features. This represents a lower limit in the estimation of the band gaps. XPS measurements were carried out at RT with a SPECS Phoibos 150 hemispherical energy analyzer using a monochromatic Al Kα X-ray source at 1486.6 eV. XPS spectra have been referenced to the Fermi level, fitted with a Fermi-Dirac distribution at the sample temperature.

First-principles calculations were performed *via* Density Functional Theory as implemented in the SIESTA package.[28,29] Here the valence electrons are described with a basis set given by a linear combination of numerical atomic-orbitals, in our case a double-ζ plus polarization (DZP) basis set with the orbital radii defined using a 50 meV energy shift.[29] We adopted for the top Au atomic layer an extended DZP basis optimized for the description of the Au(111) surface[30] as well as a Hydrogen passivation of the slab bottom layer to prevent spurious effects due to the proximity of the surface states on the slab representation.[31] Moreover, for a better description of the carbon states, the basis set was extended to included 3s and 3p orbitals.[6] The core electrons were represented by norm-conserving Troullier-Martins pseudopotentials.[32] Dispersive interactions were considered *via* the van der Waals density functional by Dion et al[33] with the modified exchange by Klimeš, Bowler and Michaelides.[34] The fineness of the grid for integrations in real space was defined using a 300 Ry energy cutoff. The self-consistency cycle was stopped when the changes of the density matrix elements were less than 10^{-5} and also lower than 10^{-4} eV for the Hamiltonian matrix elements. The smearing of the electronic occupations was defined by an electronic temperature of 300 K

with a Fermi-Dirac distribution. The structures were allowed to fully relax until the forces were lower than 10 meV/Å on top of a 3-layer thick slab within a 17.65x30.57x60 $Å^3$ simulation cell (with the two bottom layers kept fix with experimental lattice). We used a 15 k-point mesh along the GNRs periodic direction (x) and for calculations involving the Au substrate 3 k-points were adopted along the other periodic direction (y) as well. The Au surface density of states (DOS), shown in Figure 6b, was obtained by the difference between the DOS projected on the Au atoms in the surface layer and far from the GNR and the DOS projected on the Au atoms in middle slab layer, which has been shown to provide a good estimation using similar parameters.[35]

Acknowledgement

We are indebted to D. Pérez and E. Guitián for fruitful discussions. C.M. was supported by the Agency for Management of University and Research grants (AGAUR) of the Catalan government through the FP7 framework program of the European Commission under Marie Curie COFUND action 600385 funded by the CERCA Program/Generalitat de Catalunya. We acknowledge support from the Spanish Ministry of Economy and Competitiveness, MINECO (under Contracts No. MAT2016-78293-C6, FIS2017-83780-P and Severo Ochoa No. SEV-2017-0706), the European Regional Development Fund (ERDF), the Interreg V-A España-Francia-Andorra program (Contract No. EFA 194/16 TNSI), the EU project SPRING (863098), the Xunta de Galicia (Centro singular de investigación de Galicia accreditation 2016-2019, ED431G/09).

References

1. Wagner, P.; Ewels, C. P.; Adjizian, J.-J.; Magaud, L.; Pochet, P.; Roche, S.; Lopez-Bezanilla, A.; Ivanovskaya, V. V.; Yaya, A.; Rayson, M. *et al.* Band Gap Engineering via Edge-Functionalization of Graphene Nanoribbons. *The Journal of Physical Chemistry C* **2013**, *117*, 26790–26796.

2. Tan, Y.-Z.; Yang, B.; Parvez, K.; Narita, A.; Osella, S.; Beljonne, D.; Feng, X.; Müllen, K. Atomically Precise Edge Chlorination of Nanographenes and its Application in Graphene Nanoribbons. *Nature Communications* **2013**, *4*, 2646.

3. Ruffieux, P.; Wang, S.; Yang, B.; Sánchez-Sánchez, C.; Liu, J.; Dienel, T.; Talirz, L.; Shinde, P.; Pignedoli, C. A.; Passerone, D. *et al.* On-Surface Synthesis of Graphene Nanoribbons with Zigzag Edge Topology. *Nature* **2016**, *531*, 489–492.

4. Carbonell-Sanromà, E.; Hieulle, J.; Vilas-Varela, M.; Brandimarte, P.; Iraola, M.; Barragán, A.; Li, J.; Abadia, M.; Corso, M.; Sánchez-Portal, D. *et al.* Doping of Graphene Nanoribbons *via* Functional Group Edge Modification. *ACS Nano* **2017**, *11*, 7355–7361.

5. Slota, M.; Keerthi, A.; Myers, W. K.; Tretyakov, E.; Baumgarten, M.; Ardavan, A.; Sadeghi, H.; Lambert, C. J.; Narita, A.; Müllen, K. *et al.* Magnetic Edge States and Coherent Manipulation of Graphene Nanoribbons. *Nature* **2018**, *557*, 691–695.

6. Moreno, C.; Vilas-Varela, M.; Kretz, B.; Garcia-Lekue, A.; Costache, M. V.; Paradinas, M.; Panighel, M.; Ceballos, G.; Valenzuela, S. O.; Peña, D. *et al.* Bottom-Up Synthesis of Multifunctional Nanoporous Graphene. *Science* **2018**, *360*, 199–203.

7. Shekhirev, M.; Zahl, P.; Sinitskii, A. Phenyl Functionalization of Atomically Precise Graphene Nanoribbons for Engineering Inter-ribbon Interactions and Graphene Nanopores. *ACS Nano* **2018**, *12*, 8662–8669.

8. Cho, K. M.; Cho, S.-Y.; Chong, S.; Koh, H.-J.; Kim, D. W.; Kim, J.; Jung, H.-T. Edge-Functionalized Graphene Nanoribbon Chemical Sensor: Comparison with Carbon Nanotube and Graphene. *ACS Applied Materials & Interfaces* **2018**, *10*, 42905–42914.

9. Joshi, D.; Hauser, M.; Veber, G.; Berl, A.; Xu, K.; Fischer, F. R. Super-Resolution Imaging of Clickable Graphene Nanoribbons Decorated with Fluorescent Dyes. *Journal of the American Chemical Society* **2018**, *140*, 9574–9580.

10. Li, J.; Brandimarte, P.; Vilas-Varela, M.; Merino-Díez, N.; Moreno, C.; Mugarza, A.; Mollejo, J. S.; Sánchez-Portal, D.; de Oteyza, D. G.; Corso, M. *et al.* Band Depopulation of Graphene Nanoribbons Induced by Chemical Gating with Amino Groups. *ACS Nano* **2020**, *14*, 1895–1901.

11. Moreno, C.; Paradinas, M.; Vilas-Varela, M.; Panighel, M.; Ceballos, G.; Peña, D.; Mugarza, A. On-Surface Synthesis of Superlattice Arrays of Ultra-Long Graphene Nanoribbons. *Chemical Communications* **2018**, *54*, 9402–9405.

12. Keerthi, A.; Radha, B.; Rizzo, D.; Lu, H.; Diez Cabanes, V.; Hou, I. C.-Y.; Beljonne, D.; Cornil, J.; Casiraghi, C.; Baumgarten, M. *et al.* Edge Functionalization of Structurally Defined Graphene Nanoribbons for Modulating the Self-Assembled Structures. *Journal of the American Chemical Society* **2017**, *139*, 16454–16457.

13. Franc, G.; Gourdon, A. Covalent Networks through On-Surface Chemistry in Ultra-High Vacuum: State-of-the-Art and Recent Developments. *Physical Chemistry Chemical Physics* **2011**, *13*, 14283.

14. On-Surface Synthesis II: Proceedings of the International Workshop On-Surface Synthesis, San Sebastián, 27-30 June 2016. **2016**,

15. Clair, S.; de Oteyza, D. G. Controlling a Chemical Coupling Reaction on a Surface: Tools and Strategies for On-Surface Synthesis. *Chemical Reviews* **2019**, *119*, 4717–4776.

16. Hayashi, H.; Yamaguchi, J.; Jippo, H.; Hayashi, R.; Aratani, N.; Ohfuchi, M.; Sato, S.; Yamada, H. Experimental and Theoretical Investigations of Surface-Assisted Graphene Nanoribbon Synthesis Featuring Carbon–Fluorine Bond Cleavage. *ACS Nano* **2017**, *11*, 6204–6210.

17. Cai, J.; Ruffieux, P.; Jaafar, R.; Bieri, M.; Braun, T.; Blankenburg, S.; Muoth, M.; Seitsonen, A. P.; Saleh, M.; Feng, X. *et al.* Atomically Precise Bottom-Up Fabrication of Graphene Nanoribbons. *Nature* **2010**, *466*, 470–473.

18. Basagni, A.; Sedona, F.; Pignedoli, C. A.; Cattelan, M.; Nicolas, L.; Casarin, M.; Sambi, M. Molecules–Oligomers–Nanowires–Graphene Nanoribbons: A Bottom-Up Stepwise On-Surface Covalent Synthesis Preserving Long-Range Order. *Journal of the American Chemical Society* **2015**, *137*, 1802–1808.

19. Batra, A.; Cvetko, D.; Kladnik, G.; Adak, O.; Cardoso, C.; Ferretti, A.; Prezzi, D.; Molinari, E.; Morgante, A.; Venkataraman, L. Probing the Mechanism for Graphene Nanoribbon Formation on Gold Surfaces through X-ray Spectroscopy. *Chem. Sci.* **2014**, *5*, 4419–4423.

20. Moreno, C.; Panighel, M.; Vilas-Varela, M.; Sauthier, G.; Tenorio, M.; Ceballos, G.; Peña, D.; Mugarza, A. Critical Role of Phenyl Substitution and Catalytic Substrate in the Surface-Assisted Polymerization of Dibromobianthracene Derivatives. *Chemistry of Materials* **2019**, *31*, 331–341.

21. Ohtomo, M.; Jippo, H.; Hayashi, H.; Yamaguchi, J.; Ohfuchi, M.; Yamada, H.; Sato, S. Interpolymer Self-Assembly of Bottom-up Graphene Nanoribbons Fabricated from Fluorinated Precursors. *ACS Applied Materials & Interfaces* **2018**, *10*, 31623–31630.

22. Blankenburg, S.; Cai, J.; Ruffieux, P.; Jaafar, R.; Passerone, D.; Feng, X.; Müllen, K.; Fasel, R.; Pignedoli, C. A. Intraribbon Heterojunction Formation in Ultranarrow Graphene Nanoribbons. *ACS Nano* **2012**, *6*, 2020–2025.

23. Bronner, C.; Stremlau, S.; Gille, M.; Braße, F.; Haase, A.; Hecht, S.; Tegeder, P. Aligning the Band Gap of Graphene Nanoribbons by Monomer Doping. *Angewandte Chemie* **2013**, *125*, 4518–4521.

24. Cai, J.; Pignedoli, C. A.; Talirz, L.; Ruffieux, P.; Söde, H.; Liang, L.; Meunier, V.; Berger, R.; Li, R.; Feng, X. *et al.* Graphene Nanoribbon Heterojunctions. *Nature Nanotechnology* **2014**, *9*, 896–900.

25. Merino-Díez, N.; Garcia-Lekue, A.; Carbonell-Sanromà, E.; Li, J.; Corso, M.; Colazzo, L.; Sedona, F.; Sánchez-Portal, D.; Pascual, J. I.; de Oteyza, D. G. Width-Dependent Band Gap in Armchair Graphene Nanoribbons Reveals Fermi Level Pinning on Au(111). *ACS Nano* **2017**, *11*, 11661–11668.

26. Yang, L.; Park, C.-H.; Son, Y.-W.; Cohen, M. L.; Louie, S. G. Quasiparticle Energies and Band Gaps in Graphene Nanoribbons. *Physical Review Letters* **2007**, *99*, 186801.

27. Nečas, D.; Klapetek, P. Gwyddion: an Open-Source Software for SPM Data Analysis. *Open Physics* **2012**, *10*.

28. Artacho, E.; Sánchez-Portal, D.; Ordejón, P.; García, A.; Soler, J. M. Linear-Scaling *Ab Initio* Calculations for Large and Complex Systems. *physica status solidi (b)* **1999**, *215*, 809–817.

29. Soler, J. M.; Artacho, E.; Gale, J. D.; García, A.; Junquera, J.; Ordejón, P.; Sánchez-Portal, D. The SIESTA Method for *Ab Initio* Order-N Materials Simulation. *Journal of Physics: Condensed Matter* **2002**, *14*, 2745–2779.

30. García-Gil, S.; García, A.; Lorente, N.; Ordejón, P. Optimal Strictly Localized Basis Sets for Noble Metal Surfaces. *Physical Review B* **2009**, *79*, 075441.

31. Gonzalez-Lakunza, N.; Fernández-Torrente, I.; Franke, K. J.; Lorente, N.; Arnau, A.;

Pascual, J. I. Formation of Dispersive Hybrid Bands at an Organic-Metal Interface. *Physical Review Letters* **2008**, *100*, 156805.

32. Troullier, N.; Martins, J. L. Efficient Pseudopotentials for Plane-Wave Calculations. *Physical Review B* **1991**, *43*, 1993–2006.

33. Dion, M.; Rydberg, H.; Schröder, E.; Langreth, D. C.; Lundqvist, B. I. Van der Waals Density Functional for General Geometries. *Physical Review Letters* **2004**, *92*, 599–610.

34. Klimeš, J.; Bowler, D. R.; Michaelides, A. Chemical Accuracy for the van der Waals Density Functional. *Journal of Physics: Condensed Matter* **2010**, *22*, 022201.

35. Zuzak, R.; Castro-Esteban, J.; Brandimarte, P.; Engelund, M.; Cobas, A.; Piątkowski, P.; Kolmer, M.; Pérez, D.; Guitián, E.; Szymonski, M. *et al.* Building a 22-Ring Nanographene by Combining In-Solution and On-Surface Syntheses. *Chemical Communications* **2018**, *54*, 10256–10259.

Graphical TOC Entry